Inheritance without reactivation: Insights from crustal-scale analogue experiments

Anindita Samsu[1], Alexander R Cruden[1], Nicolas E Molnar[1], Roberto F Weinberg[1]

[1]School of Earth, Atmosphere and Environment, Monash University, Clayton, VIC 3800, Australia

Corresponding author: Anindita Samsu (anindita.samsu@monash.edu)

Key Points

- Analogue models show that reactivation is not the only mechanism contributing to structural inheritance.
- Extension-oblique faults can form during orthogonal rifting as a result of transtension when the basement is sufficiently anisotropic.
- The geometry of lower crustal zones of different strengths interacts with rift kinematics, impacting fault development.

Abstract

During rifting, pre-existing basement weaknesses can affect new faults in cover rocks by a mechanism that does not appear to involve reactivation. This subtle form of inheritance can significantly impact fault network architecture above laterally variable basement domains with geomechanical anisotropies. Here we use multi-layer, brittle-ductile, crustal-scale analogue experiments to study the influence of lower crustal anisotropies on fault patterns in the overlying upper crust during a single phase of orthogonal rifting. The experiments were designed to test whether lower crustal anisotropies, oriented 45° to the extension direction, can lead to the formation of rift faults that are oblique to both the imposed extension direction and lower crustal anisotropies. This work builds on previous field-based studies of the onshore Gippsland Basin (southeast Australia). Here, basin-scale (>1 km long) NE-SW to ENE-WSW trending faults, which formed during Early Cretaceous N-S or NNE-SSW rifting, are prevalent above two levels of anisotropic basement with NNE-SSW to NE-SW structural trends. Our experiments show that a pervasive, vertically layered, mm-wide lower crustal anisotropy creates “extension-oblique” rift faults in the overlying basin within the upper crust. We interpret this to arise when local strike-slip kinematics along the interfaces of mechanically contrasting materials in the lower crust combine with the regional imposed orthogonal extension, creating a transtensional regime. Our findings highlight that the geometry of lower crustal zones of different strengths interacts with rift kinematics, impacting the orientation, kinematics and spacing of new faults.

1. Introduction

Rifts form in crust that often contains pervasive fabric anisotropies (i.e., foliation) and discrete zones shear zones and faults. The influence of pre-rift structures on new rifts has been observed around the world, from reactivation of shear zones in the NE Brazilian margin (Kirkpatrick et al., 2013), northern Scotland (Phillips et al., 2016), the East African Rift System (Daly et al., 1989; Heilman et al., 2019), and the Australian Southern Margin (Gibson et al., 2013), to the deflection of rifts as they avoid stronger crustal regions, such as cratons, and propagate along mobile belts (e.g., Corti et al., 2007; Daly et al., 1989; Tommasi and Vauchez, 2001; Wilson, 1966). System-scale studies highlight the influence of pre-rift lithospheric structures and rheological variations on the along-axis orientation of entire rifts (Brune et al., 2017; Corti et al., 2007; Heron et al., 2019). However, the relationships between pre-existing crustal weaknesses and the architecture of individual basins and fault systems have received less attention.

Using aerial imagery and field observations, Wilson et al. (2010) and Samsu et al. (2019) demonstrated variations in the main orientations of brittle structures across areas that overlie different basement domains. Such a relationship potentially reflects a subtle influence from pre-existing basement structures. However, this influence may not occur due to basement reactivation, which normally results in new extensional structures that are parallel with the basement foliation, shear zones, or faults (Heilman et al., 2019; Holdsworth et al., 1997; Kirkpatrick et al., 2013; Phillips et al., 2016). Stress re-orientation near pre-existing basement structures offers some explanation for dip-slip kinematics along faults that are oblique to the extension direction (Morley, 2010; Philippon et al., 2015), which we refer to here as “extension-oblique” faults.

Extension-oblique faults are common features of oblique or transtensional rifts, where strain is accommodated by extension perpendicular to the rift trend and shear parallel to the rift trend (Withjack & Jamison, 1986). Analogue experiments of oblique rifting have shown that the orientation and kinematics of faults is controlled by the angle of obliquity between the rift trend and the relative displacement direction between the two diverging plates (Agostini et al., 2009; Corti, 2008; Withjack & Jamison, 1986). These experiments address the kinematic boundary conditions that are required to create extension-oblique rifts but not the role of crustal fabrics in their formation.

In this study, we focus on an outstanding question: What intrinsic mechanical characteristics do pre-existing basement structures need to have in order to cause the formation of extension-oblique faults that are also oblique to the pre-existing structures? We use crustal-scale analogue models to demonstrate that strain re-orientation above pre-existing anisotropies in the lower crust enables the formation of extension-oblique faults without normal or oblique reactivation of pre-existing weaknesses. The orientation of the resulting extension-oblique faults is controlled by the mechanical properties (e.g., strength) and geometry (i.e., the spacing and width of “weak zones” that create the anisotropy) of the lower crust. Our models were designed to replicate syn-rift faulting in the western onshore Gippsland Basin, southeast Australia, where extension-oblique faults are prevalent in an area that is underlain by two levels of anisotropic basement (Samsu et al., in review): Paleozoic metasedimentary rocks of the Melbourne Zone and an inferred underlying, anomalously strong Neoproterozoic–Cambrian crustal block known as the "Selwyn Block" (Cayley et al., 2002) (Fig. 1).

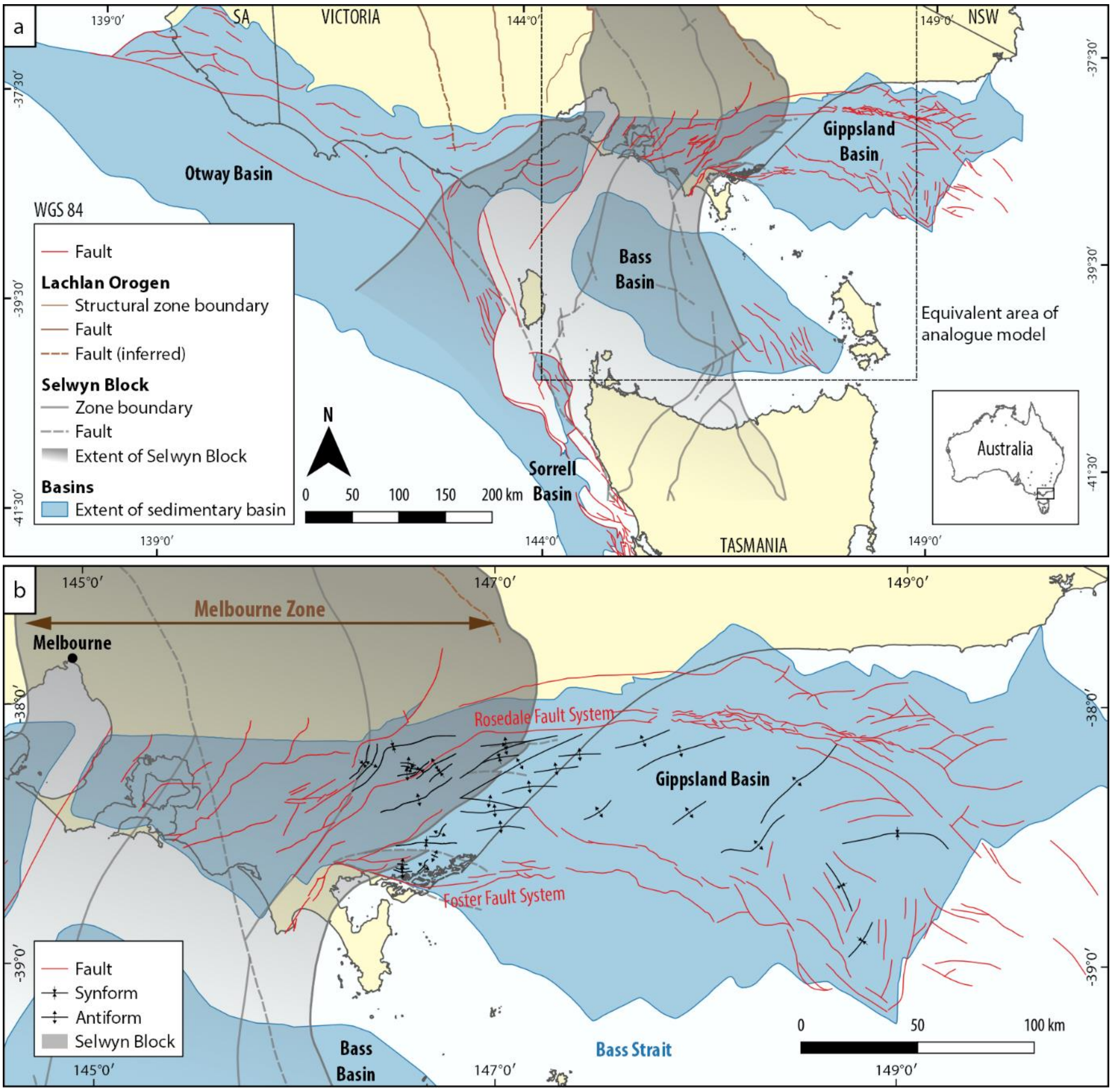

Figure 1 (a) Map of the eastern basins of the Australian Southern Margin rift system, including the Otway, Sorrell, Gippsland, and Bass basins (modified from Samsu et al., 2019). The eastern part of the Otway Basin and the western part of the Gippsland Basin is underlain by the Paleozoic Melbourne Zone (Lachlan Fold Belt) basement and the Neoproterozoic–Cambrian Selwyn Block basement (Cayley et al., 2002; McLean et al., 2010). (b) Major structures of the Gippsland Basin: Faults above the Selwyn Block/Melbourne Zone trend predominantly NE-SW and ENE-WSW, while faults east of this zone trend E-W to NW-SE (modified after Constantine, 2001 and Power et al., 2001).

2. Crustal-scale inheritance in Australia

The Neoproterozoic–Cambrian Selwyn Block was accreted onto the eastern margin of Gondwana in the Late Cambrian Delamerian Orogeny (Cayley, 2011; Cayley et al., 2002). In its current position, the Selwyn Block underlies part of the Jurassic–Cretaceous Australian Southern Margin rift system, extending from the southeast Australian mainland underneath the Bass Strait and into Tasmania (Cayley et al., 2002; Moore et al., 2016) (Fig. 1b). The presence of this heterogeneous, relatively strong, lower-crustal block may have impacted the evolution and architecture of the overlying Australian Southern Margin basins at multiple scales. At the system scale, the western margin of the Selwyn Block coincides with a deflection of the west-to-east propagating Australian Southern Margin rift system towards the south, bypassing the Bass Strait and instead continuing along the western margin of Tasmania (Fig 1a). At the basin scale, the influence of the Selwyn Block is evident in the eastern Otway Basin and western Gippsland Basin, where NE-SW to ENE-WSW trending Early Cretaceous faults are present above the Selwyn Block (Constantine, 2001; Moore et al., 2000; Norvick & Smith, 2001; Samsu et al., 2019; Willcox et al., 1992). This fault set is oblique to the inferred N-S or NNE-SSW direction of regional extension (e.g., Etheridge et al., 1985; Miller et al., 2002; Willcox and Stagg, 1990) and E-W trending orthogonal rift faults that typify areas beyond the inferred boundaries of the Selwyn Block.

Power et al. (2001, 2003) attributed the obliquity of the NE-SW to ENE-WSW faults to transtension arising from NNW-SSE directed oblique extension in the Early Cretaceous. Samsu et al. (2019, in review) used field observations from the western onshore Gippsland Basin to determine that NE-SW to ENE-WSW syn-rift faults are at acute angles to a strong, subvertical NNE-SSW trending fabric in Paleozoic basement rocks of the Melbourne Zone and the NE-SW structural grain of the Selwyn Block (Moore et al., 2016). Based on these observations, we designed experiments to simulate how the highly anisotropic, folded, and faulted turbidites of the Melbourne Zone basement may have contributed to the formation of these oblique rift faults.

3. Experimental method

Analogue modelling is a powerful tool for simulating crustal deformation in a controlled environment and testing hypotheses on its driving mechanisms, using simplified models that are scaled to a practical size (Cruden et al., 2006; Ranalli, 2001). In this study, the simplified analogue models were designed to approximately simulate an area of the onshore Gippsland Basin that straddles the postulated NE-SW trending eastern boundary of the Selwyn Block (Fig. 1). The isostatically supported, crustal-scale, brittle-ductile multilayer models were extended in one direction at a constant rate of ~4.1 cm/hr, which scales to ~2 cm/yr in nature (Fig. 2). The scaling parameters are explained in detail further below.

3.1. Boundary and initial conditions

All experiments comprised a brittle-ductile model lithosphere, with initial dimensions of 44 cm × 40 cm × 7 cm, floating isostatically on a fluid model asthenosphere contained within a 65 cm × 65 cm × 20 cm acrylic tank (Fig. 2). The simplified model lithosphere consists of a brittle upper crust, a ductile lower crust, and a ductile lithospheric mantle (Fig. 3). The natural layer thicknesses, estimated from forward modelling of geophysical potential field data (Moore et al., 2016) and seismological models (Gray et al., 1998; Kennett et al., 2013), were scaled down to model thicknesses of 1 cm for the upper crust, 2.5 cm for the lower crust, and 3.5 cm for the lithospheric mantle (Fig. 3 and Table 1).

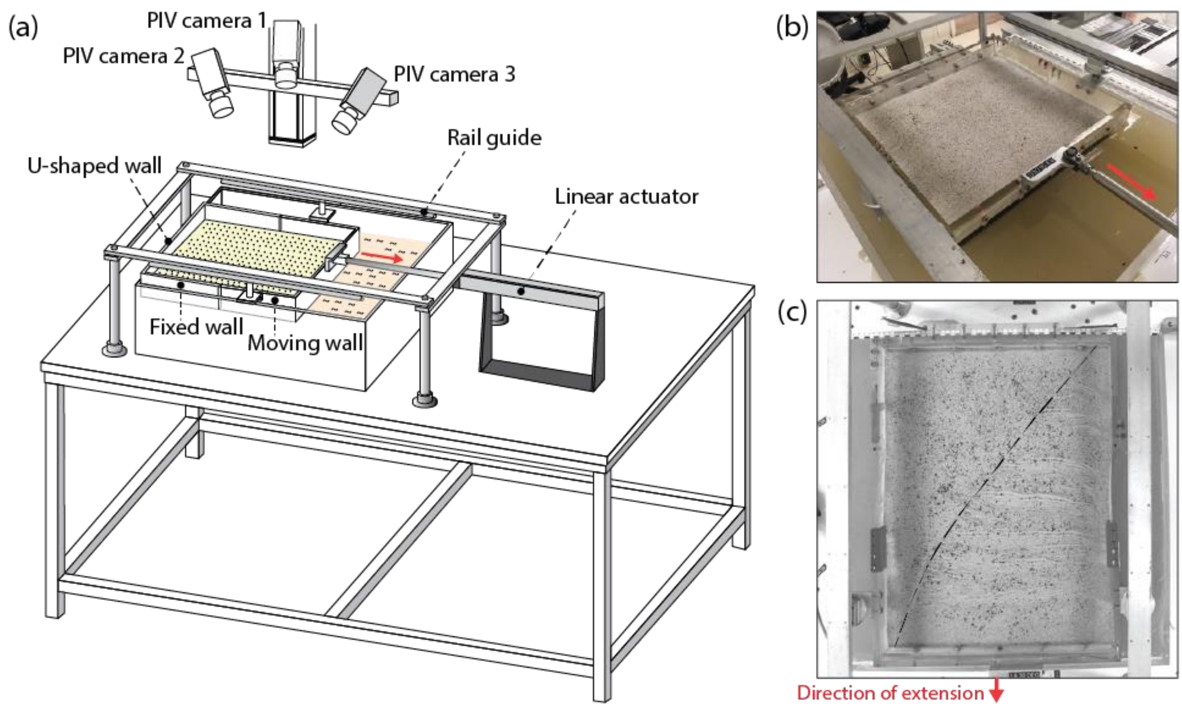

Figure 2 Experimental setup for orthogonal extension. In (a) and (b), the red arrow indicates the direction of extension. (c) Top view photograph of the model surface (Exp LE-05) at the end of the experiment. The dashed line indicates the final geometry of the strong lower crust-normal lower crust boundary (see Fig. 3 for explanation of lower crust geometries).

To model the change in fault orientations across the Selwyn Block boundary (Fig. 1), the lower crust was divided into a strong and normal domain (Fig. 3). Four experiments were carried out to test the influence of increasing the degree of anisotropy within the strong lower crust on fault orientations in the cover (see Fig. 3 for the initial lower crust geometries). All other parameters in the models remained constant.

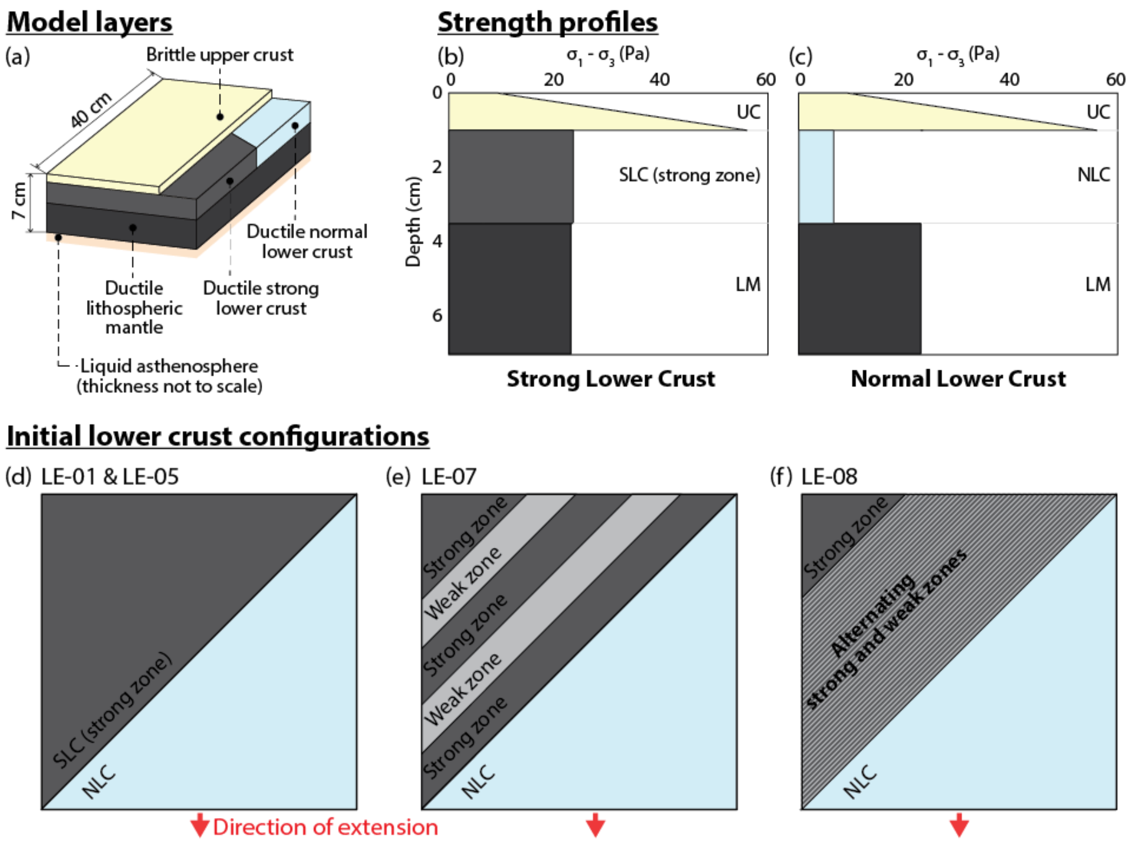

Figure 3 Structure (a) and strength profiles (b-c) of the multi-layer model lithosphere. (d–f) The configuration of the lower crust at the start of the experiments. The weak zone within the SLC is only slightly more viscous than the NLC material. UC = upper crust; SLC = strong lower crust; NLC = normal lower crust; LM = lithospheric mantle.

One side of the model was attached to a moving wall pulled by a linear actuator, imposing an orthogonal extensional boundary condition that simulates extension similar to that of N-S rifting between Australia and Antarctica in the Early Cretaceous (Miller et al., 2002). Orthogonal extension boundary conditions ensure that the formation of any faults that are oblique to the extension direction are caused by strength anisotropies in the model crust as opposed to imposed kinematic boundary conditions. Since our intention was not to force a rift (cf. Brune et al., 2017; Zwaan and Schreurs, 2017), we did not place a linear "weak zone" seed in the middle of the model.

3.2 Scaling and materials

Model parameters (e.g., length, mass, time, and velocity) and the mechanical properties of the chosen analogue materials were scaled down so that deformation occurred within a convenient time period while still behaving consistently with nature (i.e., the prototype) (Ramberg, 1967). The scaling properties used in the experiments are presented in Table 1.

Table 1 Model scaling parameters and material properties. ESPH = Envirospheres; PDMS = polydimethylsiloxane; WPL = white Plasticine; BPL = black Plasticine; K1 = hollow glass microspheres; NS = Natrosol.

		Thickness		Density		Viscosity		
		Model (mm)	Nature (km)	Model (kg/m^3)	Nature (kg/m^3)	Model (Pa s)	Nature (Pa s)	Material
Normal crust								
Upper crust	Brittle	10	10	962	2650	-	-	Sand+ESPH
Normal lower crust (NLC)	Ductile	25	25	980	2700	4.0×10^4	2.0×10^{21}	PDMS
Strong crust								
Upper crust	Brittle	10	10	962	2650	-	-	Sand+ESPH
Strong zone (lower crust)	Ductile	25	25	985	2715	5.7×10^5	2.9×10^{22}	PDMS+WPL+K1
Weak zone (lower crust)	Ductile	25	25	985	2715	7.3×10^4	3.6×10^{21}	PDMS+WPL+K1
Lithospheric mantle	Ductile	35	35	1067	2940	5.9×10^5	3.0×10^{22}	PDMS+BPL+K1
Asthenosphere	Fluid	-	-	1125	3100	380	1.9×10^{19}	NaCl-NS
Scaling factors: model/nature		$L^* = 1 \times 10^{-6}$		$\rho^* = 3.63 \times 10^{-1}$		$\eta^* = 2.0 \times 10^{-17}$		
Time scaling factor		$t^* = \eta^*/(\rho^* \cdot g^* \cdot L^*)$		$t^* = 5.5 \times 10^{-11}$		1 h in model ~ 2.1 Ma in nature		
Velocity scaling factor		$v^* = l^*/t^*$		$v^* = 1.8 \times 10^4$		41 mm/h in model ~ 20 mm/yr in nature		
Gravity scaling factor		$g^* = g_m/g_p$		$g^* = 1$				
Stress scaling factor		$\sigma^* = \rho^* \cdot L^*$		$\sigma^* = 3.63 \times 10^{-7}$				

A length scaling factor $L^* = L_m/L_p = 1 \times 10^{-6}$ was adopted (subscripts *m* and *p* refer to the model and natural prototype, respectively), so that 1 cm in the model represents 10 km in nature. The 44 cm × 40 cm surface area of the model therefore corresponds to a 440 km × 400 km area in nature (Fig. 1). The scaling factor for density ρ^* was set to 3.63×10^{-1}. The experiments were run under normal gravitational acceleration, so that the scaling factor for acceleration due to gravity $g^* = 1$, which gives a scaling factor for stress $\sigma^* = \rho^* \times g^* \times L^* = 3.63 \times 10^{-7}$ (Ritter et al., 2016). Granular materials were used to model the strong, brittle upper crust, while the ductile lower crust and lithospheric mantle were represented by mixtures of viscous materials, resulting in Christmas tree-like strength profiles (Fig. 3) that are comparable with simplified strength profiles for natural continental lithosphere under extension (Benes & Davy, 1996).

A mixture of dry granular materials with a bulk density $\rho_b = \rho_m \approx 960$ kg/m^3 was prepared to approximate a scaled natural density of $\rho_p = 2{,}650$ kg/m^3 for the upper crust. We used a mixture of dry quartz sand ($\rho_b = 1{,}580$ kg/m^3) and hollow ceramic Envirospheres® BLF and BL150 ($\rho_b \approx 390$ kg/m^3) with mass percentages of ~77.9%, 21.2%, and 1.9%, respectively, similar to Molnar et al. (2017). The internal friction angle $\phi < 38°$ and very low cohesion value $c \sim 9$ Pa of this material, measured by Molnar et al. (2017) using a Hubbert-type shear apparatus, makes it a suitable analogue for modelling brittle upper crust with a Mohr-Coulomb behavior (e.g., Byerlee, 1978; Davy & Cobbold, 1991; Mandl et al., 1977; Schellart, 2000). The quartz sand is characterized by a homogeneous grain size distribution, with ~73% of the grains falling in the 150–300 μm range.

We used polydimethylsiloxane (PDMS) and PDMS mixtures to model the ductile lower crust. PDMS is a transparent, high viscosity, high molecular weight silicone polymer frequently used in analogue modeling (Cruden et al., 2006; Molnar et al., 2017, 2018; Pysklywec & Cruden, 2004). It has a density $\rho_\mathrm{m} \approx 980$ kg/m^3, which scales to a natural lower crust density $\rho_\mathrm{p} \approx 2700$ kg/m^3. Our PDMS (Wacker Elastomer NA) approximates a Newtonian fluid with a viscosity $\eta \approx 4 \times 10^4$ Pa s. The PDMS mixtures have a slightly non-Newtonian rheology (n > 1) defined by the power law:

$$\sigma^n = v\dot{\varepsilon}$$

where σ is stress, n is the power law exponent of the material, v is a material constant (viscosity prefactor), and $\dot{\varepsilon}$ is the strain rate (Cruden et al., 2006). For example, the power law exponent for the model lithospheric mantle (LM) mixture is $n_{\mathrm{LM}} = 1.25$ (Molnar et al., 2017), making it nearly Newtonian.

The lower crust layer is divided into two triangular domains separated by a vertical interface 45° to the extension direction (Fig. 3d–f), consistent with the orientation of the NE-SW boundary and structural trend of the Selwyn Block in the corresponding area in nature (Fig. 1). One triangular domain of "strong" lower crust (SLC) approximates the Selwyn Block. The "strong zone" material within the SLC (Fig. 3) is a mixture of PDMS, modeling clay (white Colorific Plasticine®), and 3M® K1 hollow glass microspheres (e.g., Cruden et al., 2006; Molnar et al., 2017; Riller et al., 2012). Combining the PDMS with modeling clay increases its effective viscosity and density, while adding glass microspheres reduces its density and increases its effective viscosity. The relative amounts of the three components were adjusted to a mixture with 61.0 vol% PDMS, 16.9 vol% white Plasticine®, and 22.1 vol% microspheres, giving a density ρ = 985 kg/m^3 and an effective viscosity of ~ 5.7 × 10^5 Pa s (at our experimental strain rate of 1.0 × 10^{-4} s^{-1}) and scaling to a natural density of ρ = 2715 kg/m^3 and natural viscosity of 2.9 × 10^{22} Pa s. The rheological properties of the PDMS mixture were measured using an Anton Paar Physica MCR-301 parallel plate rheometer. The experimental strain rate was estimated by dividing the velocity of the linear actuator (i.e., the rate at which the model was extended) by the total initial model thickness of 7 cm (Benes & Scott, 1996).

The strong zone material is one order of magnitude more viscous than the neighboring "normal" lower crustal (NLC) triangular domain, which consists of pure PDMS (~ 4.0 × 10^4 Pa s). Anisotropies within the SLC are reproduced by incorporating linear "weak zones" (Fig. 3) using a PDMS mixture consisting of 80.9 vol% PDMS, 9.0 vol% white Plasticine®, and 10.1 vol% microspheres. This material has an effective viscosity of ~ 7.3 × 10^4 Pa s, hence only slightly more viscous than the NLC material. In the reference experiment (Exp LE-01), the SLC/strong zone material (Fig. 3) was substituted by the weak zone material to assess whether a slight contrast in viscosity has an effect on strain localization or rotation (Section 4.1).

The model lithospheric mantle is a mixture of PDMS, modeling clay (black Colorific Plasticine®), and 3M® K1 hollow glass microspheres (ρ = 125 kg/m^3). We used a mixture of 55.8 vol% PDMS, 29.7 vol% black Plasticine®, and 14.6 vol% microspheres to achieve a density ρ_m = 1067 kg/m^3 and effective viscosity of 5.9 × 10^5 Pa s, corresponding to an upscaled density ρ_p = 2940 kg/m^3 and viscosity of 3.0 × 10^{22} Pa s.

The model asthenosphere is a mixture of Natrosol® 250 HH, NaCl (sodium chloride), formaldehyde, and deionized water (Boutelier et al., 2016; Molnar et al., 2017). Natrosol® hydroxyethylcellulose is a water-soluble polymer that can used to modify the viscosity of an aqueous solution without significantly affecting its density (Boutelier et al., 2016). Natrosol® acts as a Newtonian fluid under shear strain rates typically employed in experimental tectonics (Boutelier et al., 2016). The model asthenosphere mixture has a viscosity μ_m = 380 Pa s, scaling to a prototype viscosity μ_p = 1.9 × 10^{19} Pa s, which is comparable with natural viscosity estimates for the asthenosphere (Artyushkov, 1983; Ranalli, 1995). The mixture has a density ρ_m = 1,125 kg/m^3 (Molnar et al., 2017), equivalent to a natural density $\rho_p \approx$ 3,100 kg/m^3 (e.g., Pysklywec and Cruden, 2004).

3.3 Construction of the model layers

The ductile lower crust and lithospheric mantle were constructed to fit within the pair of U-shaped walls (Fig. 2). These ductile layers were molded into rigid frames on top of a flat surface (Fig. 4). They were placed within the frames ~72 h before the start of the experiment to allow enough time for the material to fill up the frames, settle, and expel trapped air bubbles. Because the lower crust layer comprised two strength domains, the two ductile lower crust domains (the SLC and the NLC) were molded separately in two rigid frames (Fig. 4a). When the mixtures had settled, the two pieces were put together to form the final rectangular-shaped lower crust layer. Beforehand, a 80:20 wt% paraffin oil and petrolatum jelly mixture (Duarte et al., 2014) was smeared onto the SLC-NLC interface to keep the two materials separate. However, this had a negligible effect on strain localization during the experiments, as the mixture may have reacted chemically with Plasticine (Duarte et al., 2014) and lost its lubricating effect.

During preparation of the SLC domain for Exp LE-07, which involve 5.4 cm-wide weak zones, the areas that were to be filled with the weaker material were cut with a knife and removed from the already molded strong zone material. The cut interfaces were kept vertical by placing thin, rigid plastic sheets where the cuts were made. The “gaps” were then filled with the weak zone material. The plastic sheets were removed once the weak zone material had settled. Similarly, preparation of the SLC domain of Exp LE-08 required extra steps shown in Fig. 4. Linear weak zones were incorporated into the model lower crustal layer at an angle of 45° relative to the extension-perpendicular walls. The rheological boundary between the SLC and NLC also has the same 45° orientation and crosses the center of the model in map view (Fig. 4e).

Specially designed 4 cm wide horizontal grips were attached to the lithospheric mantle layer (Fig. 4b); the grips were later fastened to the sides of the U-shaped walls that are perpendicular to the extension direction. The lithospheric mantle (along with the horizontal grips) and lower crust were placed in the tank and allowed to settle over a period of ~24 h, allowing sufficient time for the model to achieve isostatic equilibrium and for air bubbles to dissipate. A 80:20 wt% paraffin oil and petrolatum jelly mixture was used as a lubricant between the lateral boundaries of the model and the U-shaped walls to minimize boundary effects caused by friction.

Shortly before the start of the experiment, the model upper crust layer was deposited on top of the model lower crust by slow sifting the prepared granular mixture from a height of ~10 cm. The surface of the upper crust layer was not flattened or scraped off in order to avoid alterations in the mechanical properties of the layer (e.g., localized compaction). Fine coffee grounds were sifted onto the surface of the model to serve as passive markers during deformation monitoring (see Section 3.4). Once all layers of the model lithosphere were in place, the horizontal grips were fastened to the extension-perpendicular sides of the U-shaped walls.

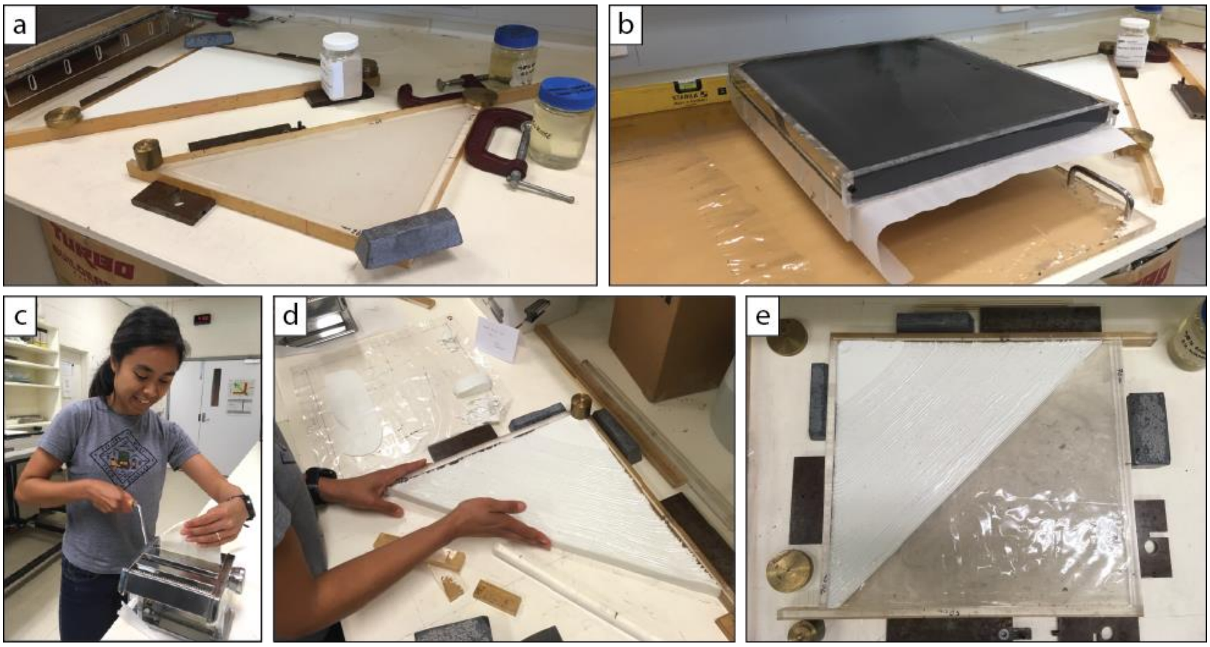

Figure 4 Photographs of the preparation of the ductile lower crust and lithospheric mantle layers. (a) The SLC (strong zone) and NLC material were placed in separate rigid frames on top of a flat workbench; the two parts were united to form the lower crust once the mixtures had settled. (b) The lithospheric mantle material was placed into a rectangular rigid frame and attached to horizontal grips. Flattening of this layer was facilitated with a rolling pin. (c–e) Assembly of the lower crust layer for Exp LE-08. A pasta maker was used to uniformly flatten strong zone and weak zone materials to a thickness < 2 mm (c). For the assembly of the SLC domain, they were cut into strips and placed vertically in an alternating manner within the rigid frame (d), after which this domain was attached to the NLC domain (e). Photographs (c–e) courtesy of J. Samsu.

3.4 Deformation monitoring and analysis

Deformation in the upper crust layer was monitored during the experiment by stereoscopic particle imaging velocimetry (PIV) (Adam et al., 2005), so that the resulting strain distribution and fault orientations could be characterized over time. The PIV system comprises three high-speed cameras that provide a spatial resolution ≥ 1 mm and a temporal resolution ≥ 0.1 s (Molnar et al., 2017). Successive images were recorded at 15 s intervals during each experimental run. Surface strain and topographic data was derived following the workflow of Molnar et al. (2017). The incremental displacement field was computed using stereo cross correlation, forming the basis for deriving the strain tensor components,

$$E_{ij} = \frac{\partial V_i}{\partial_j} \; with \; i \in \{x, y, z\} \; and \; j\{x, y, z\}$$

where E_{ij} describes the gradient in the vector component *i* along the *j* axis (Adam et al., 2005), and *V* is the velocity vector. The scalar fields were used to derive incremental normal and shear strain as well as the height of the model surface, or digital elevation model (DEM). The cumulative strain was calculated as the sum of the incremental strain and used to produce a grid of finite strain ellipses. The maximum normal strain on the surface, E_{surf}, was derived from the larger eigenvalue of the 2D strain matrix

$$\begin{vmatrix} E_{xx} & E_{xy} \\ E_{yx} & E_{yy} \end{vmatrix}$$

and the relationship

$$E_{surf} = \frac{(E_{xx} + E_{yy})}{2} + \sqrt{\frac{(E_{xx} + E_{yy})^2}{4} + \frac{(E_{xy} + E_{yx})^2}{4}}$$

A local coordinate system was chosen such that the *z*-direction is aligned with the surface normal. *Exx* and *Exy* are partial derivatives of the velocity components $\partial Vx/\partial x$ and $\partial Vx/\partial y$, and *Eyx* and *Eyy* are partial derivatives of the velocity components $\partial Vy/\partial x$ and $\partial Vy/\partial y$. Strain maps, complemented with DEMs and top-view photographs of the model surface (illuminated with oblique lighting) enabled us to track the nucleation, growth, and distribution of faults at different stages of the experiments. At the end of each experiment, the granular upper crustal material was removed with a vacuum cleaner and the top surface of the lower crustal material was photographed to document the final geometries of the lower crustal rheological boundaries.

4. Results

We present the results of four experiments: one reference experiment (Exp LE-01; see S1 and S2 in supporting information), where the lower crust is made up of two mixtures of similar rheology, and three other experiments (Exp LE-05, LE-07, and LE-08; Fig. 5), where the arrangement of weak zones within the SLC domain is varied to represent different wavelengths of basement anisotropy (Fig. 3). When viewing the models in map view, the upper side of the image is referred to as “north”, and the model is being extended towards the “south”. In describing the fault patterns, the upper crust is divided into two domains: a NW domain, underlain by the SLC (with or without weak zones), and a SE domain, which overlies the NLC (Fig. 5). Faults near the western and eastern boundaries of the models curve towards parallelism with the model edges. This boundary effect results from friction between the model’s lateral boundaries and the confining U-shaped walls. It affects a small area outside the central region of interest.

4.1 Reference experiment: quasi-homogeneous lower crust (Exp LE-01)

In the reference experiment LE-01, we tested the influence of two homogeneous lower crustal domains of slightly different viscosities on upper crustal fault patterns during orthogonal extension (S1 and S2 in supporting information). The upper crust across the entire model area developed an E-W trending horst and graben system. Based on the DEM, E-W trending normal faults began to nucleate by ~0.3 h (3% extension). As extension progressed, the faults propagated both westwards and eastwards. They reached their final length at ~2 h (21% extension), after which strain was accommodated by widening of the graben. The orientation of the faults was not influenced by the presence of the oblique SLC-NLC interface. This suggests that the viscosity contrast between the SLC and NLC in this experiment was negligible and that a higher viscosity contrast is required for two adjoining rheologically different lower crustal domains to influence the orientation of rift faults during orthogonal extension.

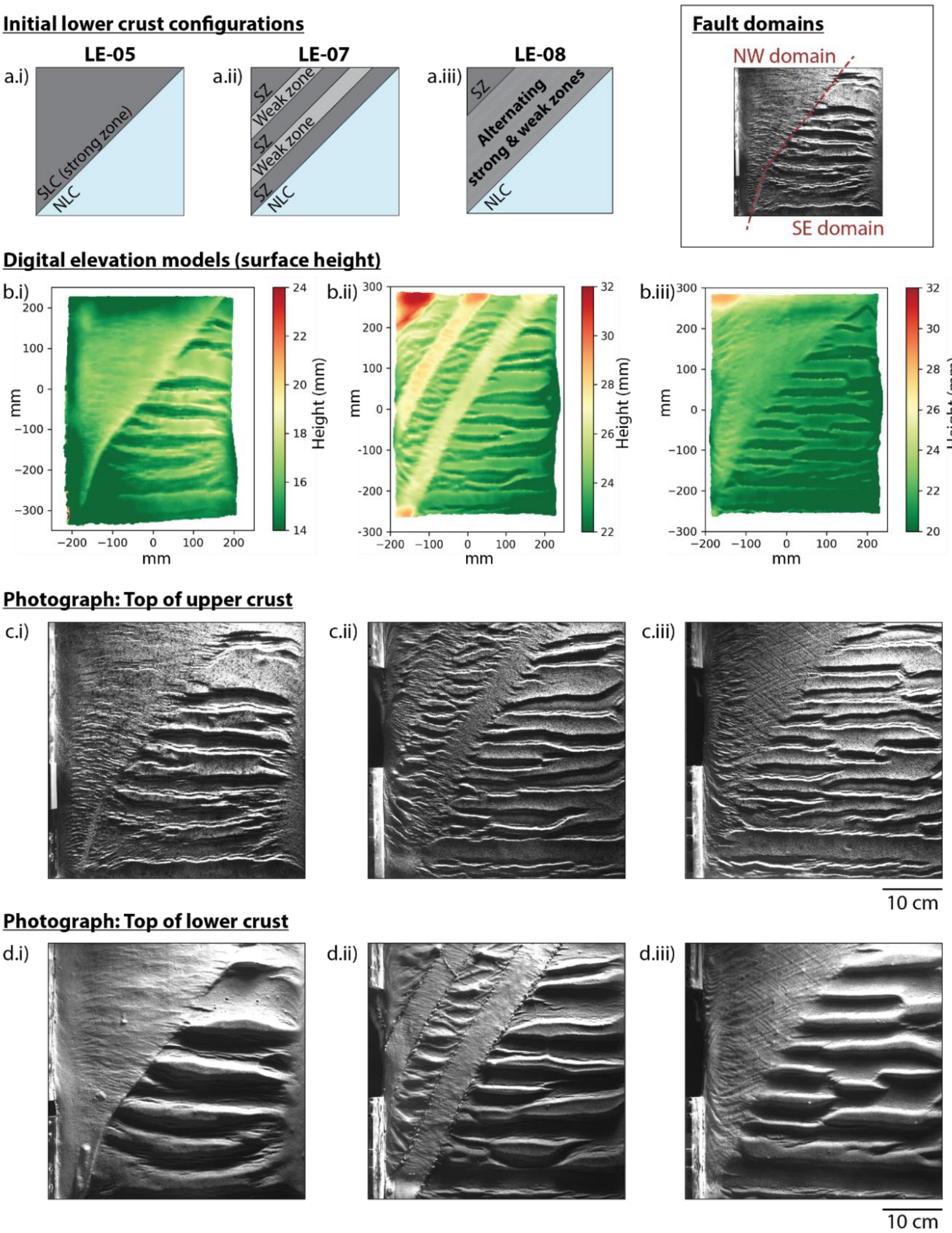

Figure 5 Results of orthogonal extension experiments at 4.5 h (47% strain) in map view, with no anisotropy (a.i), 5.4 cm-wide weak zones (a.ii), and ~2 mm-wide weak zones (a.iii) in the strong lower crustal block. (b) DEM (in mm) from photogrammetric PIV data; (c) photograph of surface of upper crust; (d) photograph of surface of lower crust. The top right inset shows the position of the NW and SE domains. SLC = strong lower crust; NLC = normal lower crust; SZ = strong zone.

4.2 Strong vs. normal lower crust (Exp LE-05)

The lower crust in Exp LE-05 has the same initial geometry as the reference experiment. However, the SLC material (with an effective viscosity of ~ 5.7×10^5 Pa s) is one order of magnitude more viscous than the adjacent NLC (~ 4.0×10^4 Pa s). The effect of this strength contrast is apparent in the distinct styles of faulting above the two domains (Fig. 5b.i and 5c.i). The SE domain is characterized by an E-W trending horst and graben system. Strain was localized along oppositely dipping faults which formed at early stages (~0.8 h; 8% strain) and were spaced ~3 to 4 cm apart by the end of the experiment (Movies S3 and S4 in supporting information). The faults reached their final length at ~1.3 h (13% strain), when their lateral propagation was arrested at the model boundary and the diagonal SLC-NLC boundary. As extension progressed, the grabens deepened as throw along the bounding faults increased. Once the boundary faults had propagated to the bottom of the brittle upper crust, strain was accommodated by widening of the graben.

In the NW domain, strain in the upper crust was more distributed, resulting in short, <1 mm-spaced faults (Fig. 5c.i). The faults initially formed in the south (~1.4 h; 15% strain) and then began nucleating in the north, near the model center (~2.0 h; 21% strain) as extension progressed. By the end of the experiment, faults above the strong lower crust had not linked together via relay structures, so that their length remained shorter than the faults in the SE domain (Fig. 5c.i). Most of the faults in the NW domain are E-W, but those within ~30 mm of the SLC-NLC boundary trend WNW-ESE, curving to approach perpendicularity to the boundary.

4.3 Wide anisotropy in the strong lower crust (Exp LE-07)

The overall evolution and final pattern of faults in the SE domain in Exp LE-07 and LE-08 (Section 4.4) are very similar to the horst-and-graben style of faulting in the SE domain of Exp LE-05. In Exp LE-07, the fault pattern in the NW domain is influenced by the presence of two linear weak zones which are 5.4 cm wide and spaced 5.4 cm apart (Fig. 5a.ii and 5b.ii). Faults above the weak zones form grabens bound by oppositely dipping, E-W trending faults, comparable to the style of faulting in the SE domain (Fig. 5c.ii). The spacing of these faults appears to be intermediate between two end members of fault localization (i.e., highest degree of localization above the NLC and even distribution above the SLC). NW-SE trending faults above the SLC are evenly distributed and narrowly spaced.

In the top view photographs of the upper crust surface (Movie S5 in supporting information), E-W trending faults in the SE domain had begun forming by ~0.8 h (8% strain). E-W trending faults above the weak zones within the NW domain began forming at ~1.1 h (11% strain). Faults above strong zones within the NW domain began forming at ~2.0 h (21% strain), first nucleating at the boundaries of the weak zones and then propagating inwards, orthogonal to the lower crustal domain boundaries.

The formation of NW-SE trending faults above the strong zones and E-W trending faults above the weak zones within the NW domain were controlled by the widely spaced anisotropy in the underlying lower crust (Fig. 6). This experiment demonstrates that strain partitioning resulted from the presence of extension-oblique zones of highly contrasting strengths, simulated by large viscosity differences in the models. Finite strain ellipses at the end of this experiment exhibit a N-S maximum stretching direction in the SE domain and weak zones in the NW domain (consistent with the imposed N-S extension) and a NNW-SSE maximum stretching direction above the SLC in the NW domain (Fig. 6a).

4.4 Narrow anisotropy in the strong lower crust (Exp LE-08)

In Exp LE-08, we implemented a higher degree of anisotropy than in Exp LE-07 by creating narrowly spaced, ~2 mm-wide weak zones within the SLC, separated by ~2 mm-wide SLC material (Fig. 5a.iii). In the top view photographs of the upper crust surface (Movie S7 in supporting information), E-W trending faults in the SE domain began forming by ~0.8 h (8% strain). Faults in the NW domain began forming at ~1.4 h (15% strain) near the model's western edge. Two sets of narrowly spaced faults, trending NW-SE and ENE-WSW, began forming at ~3.1 h (32% strain) (Fig. 7). Both of these coeval fault sets are oblique to the N-S extension direction and the NE-SW trending anisotropy and SLC-NLC boundary. The two sets form an apparently conjugate or orthorhombic pattern, with an acute bisector trending WNW-ESE (100°) (Fig. 8b). The obtuse bisector trends NNE-SSW (10°), deviating slightly from the imposed N-S extension. The ENE-WSW trending set is more pronounced than the WNW-ESE trending set because they exhibit greater dip-slip displacement. Finite strain ellipses at the end of this experiment exhibit a N-S maximum stretching direction in the SE domain and a NNW-SSE maximum stretching direction in the NW domain (Fig. 7a).

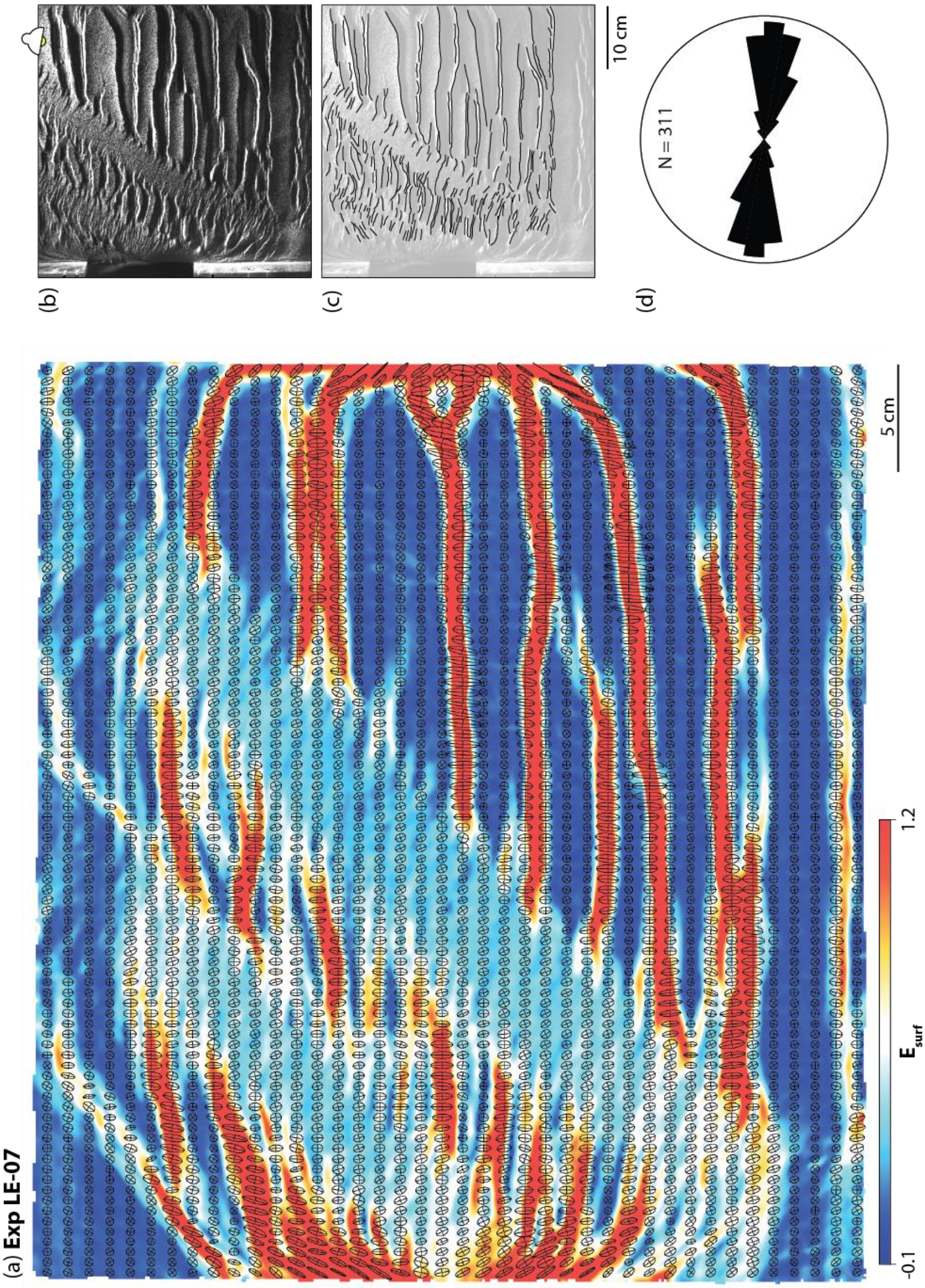

Figure 6 Results from Exp LE-07: (a) cumulative maximum normal strain on surface at the end of the experiment, overlain by 2D strain ellipses; (b) top view photograph of upper crust surface illuminated at an angle from the north indicated by the lamp on the figure; (c) fault traces; and (d) rose diagram of fault traces. Note rotation of fault orientation at the boundaries between weak and strong zones. For the evolution of the cumulative strain, see Movie S6 in the supporting information.

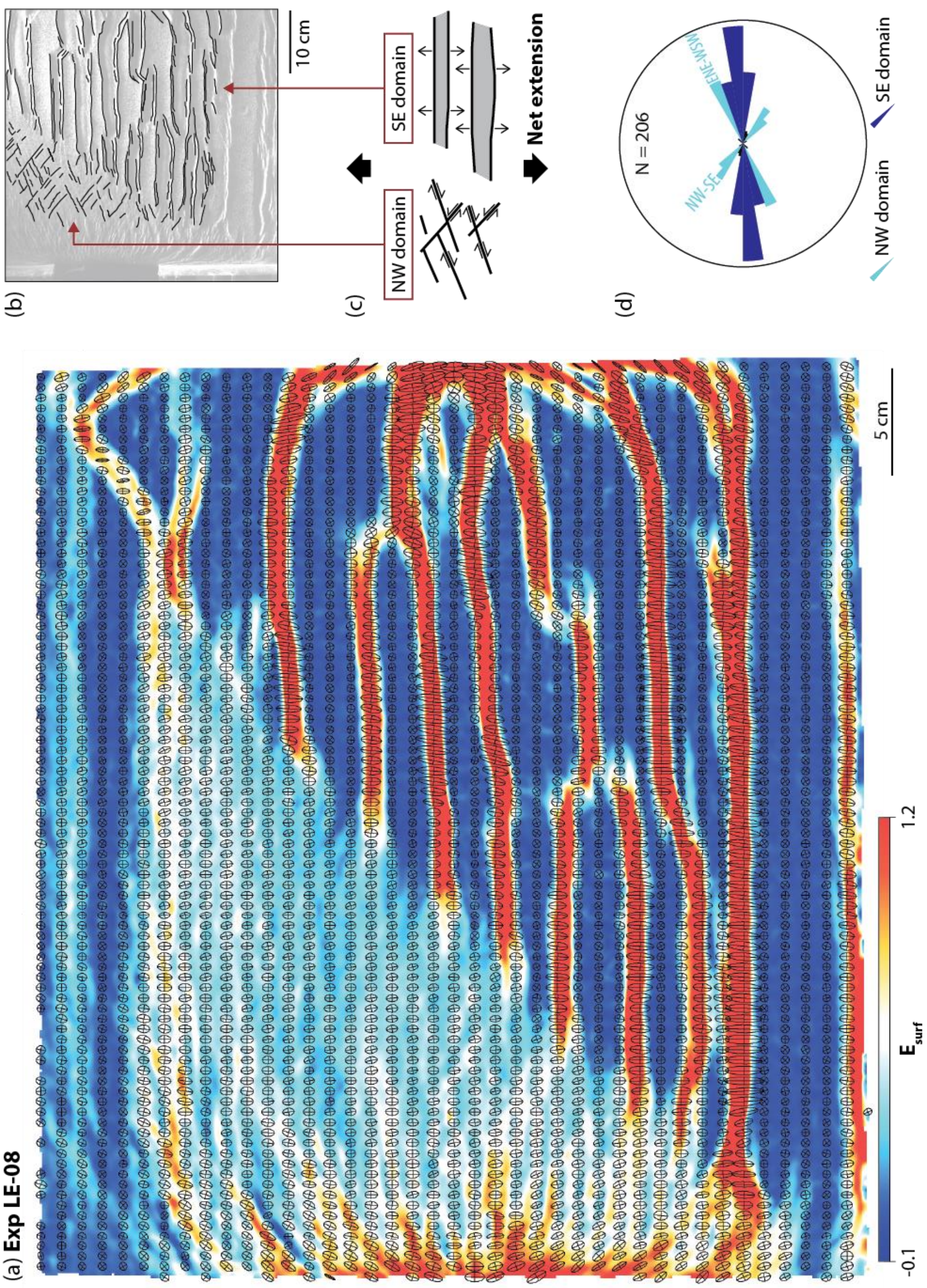

Figure 7 Results from Exp LE-08: (a) cumulative maximum normal strain on surface at the end of the experiment, overlain by 2D strain ellipses; (b) fault traces overlain on top-down photo of upper crust surface, (c) schematic plan view illustration of the accommodation of N-S extension by an orthorhombic fault set in the NW domain and E-W faults in the SE domain, and (d) rose diagram of fault traces. For the evolution of the cumulative strain, see Movie S8 in the supporting information.

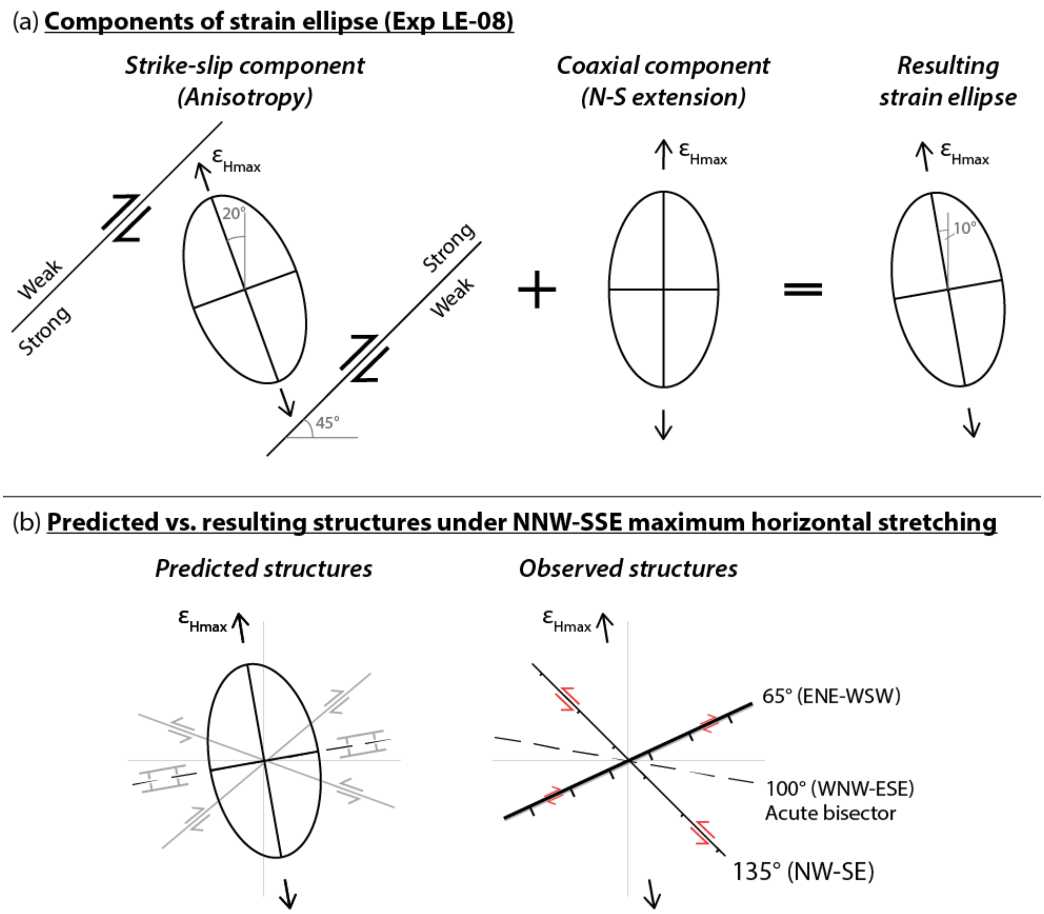

Figure 8 Schematic illustration of deformation and associated kinematics in the NW domain of Exp LE-08. (a) The representative strain ellipse can be broken down into a strike-slip (non-coaxial) and coaxial component. These representative 2D strain ellipses are not to scale; the relative contributions of the strike-slip and coaxial component may be different in the experiment. (b) Comparing the predicted structures (under a NNW-SSE maximum horizontal stretching direction ε_{Hmax}) with the resulting faults at the upper crust surface at the end of the experiment. The reason for this discrepancy is an effect unaccounted for in the simple prediction (see Section 5.3 for explanation). The observed ENE-WSW trending faults are wider than NW-SE faults, suggesting that they have accommodated a significant amount of dip-slip displacement (greater than strike-slip displacement).

Although the fault populations in the NW and SE domains exhibit different orientations, both patterns formed as products of the same imposed N-S directed bulk extension (Fig. 7b and 7c). Parallel, E-W trending faults in the SE domain represent extension-orthogonal normal faults that are consistent with formation in an Andersonian normal faulting regime. In contrast, the orthorhombic fault pattern in the NW domain signifies a local change in the strain field due to the role of the pervasive anisotropy in the lower crust. Because these faults must accommodate the bulk N-S extension, we infer that these oblique fault sets must have a strike-slip component as indicated in Figure 7c.

5. Discussion

Upper crustal deformation in our experiments was influenced by re-orientation of the stress and strain fields across the SLC, as there were no weak layers that separated the upper and lower crust layers (cf. "attached stress regime" in Bell, 1996). As a result, faults in the brittle upper crust were localized above areas of necking and thinning in the ductile lower crust (compare Fig. 5c and 5d).

5.1 The influence of crustal strength on fault spacing

In Exp LE-05, the NW domain is populated by short, closely spaced faults, while the SE domain experienced a higher degree of strain localization evidenced by widely spaced grabens, bounded by long faults with large displacements (Fig. 5a). Similarly, the spacing of faults in the NW domain above the weak zones of Exp LE-07 is greater than between faults above the strong zones, but less than the spacing between faults in the SE domain (Fig. 5b). These observations are consistent with numerical models of extensional systems (Sharples et al., 2015; Wijns et al., 2005) and analogue models of contractional tectonics (Riller et al., 2012; Schueller & Davy, 2008), which suggest that the strength ratio between the strong, brittle upper crust and the weaker, ductile lower crust controls the degree of strain localization. In our experiments, this ratio is controlled by the viscosity of the lower crust material.

5.2 Rotation of strain axes above a strong, anisotropic lower crustal block

Despite the orthogonal extension boundary condition in our experiments, our models simulate transtension due to the presence of NE-SW trending anisotropies in the lower crust. The deformation observed in the brittle upper crust reflects deformation in the underlying lower crust, which is governed by ductile flow (Fossen & Tikoff, 1998). The obliquity of faults in the NW domain of Exp LE-07 and LE-08 suggests that the model crust did not experience pure shear during extension.

Calculated finite strain ellipses at the end of Exp LE-08 (Fig. 7) exhibit a N-S maximum stretching direction ε_{Hmax} in the SE domain. The NW domain is populated by strain ellipses with a NNW-SSE ε_{Hmax}, deviating slightly from N-S. We infer that the 2D horizontal strain ellipses reflect the superposition of a coaxial strain component (the N-S imposed extension on the system) and a strike-slip component arising from dextral motion along the oblique, 45° pervasive anisotropy within the layered SLC and along the SLC-NLC interface (Fig. 8a). Therefore, the model crust must have undergone bulk sinistral transtension. Within each narrow strong zone in the NW domain, strike-slip kinematics at the interfaces between the strong and weak materials resulted in internal sinistral shearing and therefore an anti-clockwise rotation of the strain ellipse.

From the NNW-SSE trending ε_{Hmax}, we expected ENE-WSW trending normal faults or a conjugate set of faults with an ENE-WSW trending acute bisector to form in the NW domain (Fig. 8b). Instead, strain in this domain is accommodated by an orthorhombic fault system, where the ENE-WSW set is dominant. We infer that the ENE-WSW faults have a significant dip-slip offset and a minor strike-slip offset. A less dominant NW-SE fault set with a significant strike-slip component and a minor dip-slip component must also form to maintain strain compatibility (e.g., Fossen & Tikoff, 1998). The reason for the discrepancy between the observed and predicted fault patterns is an effect unaccounted is outlined in detail in Section 5.3.

The presence of alternating 5.4 cm-wide strong and weak zones in the NW domain of Exp LE-07 resulted in strain partitioning. Maximum horizontal stretching, ε_{Hmax}, trends N-S above the weak zones within the NW domain (Fig. 6), resulting in E-W trending faults. The NNW-SSE trending ε_{Hmax} is confined to the strong zones. In this experiment, E-W trending faults first nucleated and propagated in the SE domain and in the weak zones of the NW domain until they reached the interfaces with the strong zones; NW-SE trending faults then propagated from the interfaces and into the center of the strong zones. We interpret that the strong zones acted as transfer zones (cf. Zwaan and Schreurs, 2017), across which older faults in the SE domain and in the NW domain weak zones linked up via extension-oblique faults (Fig. 9a). To maintain strain compatibility, these NW-SE trending faults are likely to have a sinistral strike-slip component.

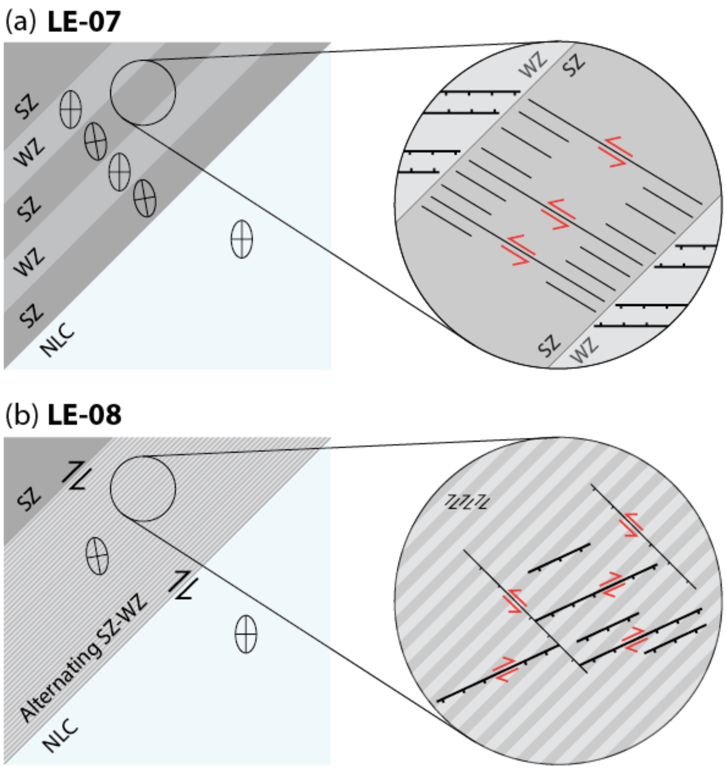

Figure 9 (a) Strain partitioning in the NW domain of Exp LE-07. The 2D strain ellipses are rotated anticlockwise in the strong zones, but they remain consistent with the NLC in the weak zones. (b) Strike-slip movement along all strong-weak interfaces in the NW domain of Exp LE-08 results in an "averaging effect" of the anisotropic properties of the lower crust. Hence the strain ellipse is rotated anticlockwise across the entire NW domain. SZ= strong zone; WZ = weak zone.

5.3 The scale-dependent role of lower crustal anisotropies on fault patterns

The different characteristics of extension-oblique faults in Exp LE-07 (above the strong zones in the NW domain) and LE-08 are attributed to the geometry of the lower crustal anisotropies, which interacted with the imposed boundary conditions. While certain structures would have been expected given the NNW-SSE maximum horizontal stretching (Fig. 8b), the role, kinematics and intensity of faults above the different strong and weak regions were modified by: (i) the 45° angle between the imposed N-S stretching and the boundaries between strong and weak zones, along which local strike-slip movement occurred (Fig. 9), and (ii) the spacing and width of the alternating strong and weak zones. This geometric influence is exemplified by faults in the NW domain of Exp LE-07 (Fig. 6). Here, E-W trending faults above the weak zones forced the dominance of NW-SE trending transfer faults above the strong zones (as opposed to NE-SW trending faults), which link the E-W faults and accommodate extensional strain.

Exp LE-07 and LE-08 represent two end member scenarios where either: (a) strain is partitioned between zones of contrasting strength within an anisotropic lower crustal block (Fig. 9a), or (b) the properties of zones of contrasting strength are "averaged" (Fig. 9b). Exp LE-08 demonstrates that a lower crustal block, with a stronger average viscosity than the adjacent block and containing a vertical, closely spaced, and pervasive anisotropy, will behave as a single block (Fig. 9b). When the width of the alternating weak and strong zones is below a certain threshold, rotation of the strain axes occurs not just at the strong-weak zone interfaces, but across the entire NW domain. When the width of the anisotropy is increased, alternating weak and strong zones within the SLC will tend to act as discrete lower crustal blocks with their own distinct mechanical properties, as opposed to being part of a pervasive fabric within a single block. Quantifying the threshold width of the anisotropies is beyond the scope of this study, but it is likely to be controlled by the viscosity ratio between the strong and weak zones, the ratio between the brittle crust thickness and the width of the anisotropy, and the minimum resolvable fault displacement in the experimental setup.

5.4 Model limitations and implications for natural rift basins

Basin-scale (>1 km long) ENE-WSW trending normal faults in the western onshore Gippsland Basin (Samsu et al., 2019) were replicated in the NW domain of Exp LE-08 by introducing closely spaced anisotropies representing the folded and faulted Melbourne Zone basement. However, the analogue experiment also produced NW-SE trending faults which are not represented in the basin-scale fault map interpreted from geophysical potential field data. If such NW-SE faults were present, their lateral and dip-slip displacement may have been too small to generate gravity and magnetic anomalies. Outcrop-scale NNW-SSE faults and fractures are present in the Cretaceous Strzelecki Group rocks, but their formation has been attributed to later periods of contraction as opposed to rifting (Samsu et al., 2019).

While our results do not fully replicate fault patterns in the western onshore Gippsland Basin, our experiments provide insight into the crustal-level anisotropies that are required for the formation of extension-oblique structures during rifting without reactivation of basement faults. They also demonstrate the influence of a transverse, anomalously strong, anisotropic crustal block on rift basin architecture, as opposed to the more widely explored role of crustal weaknesses (e.g., Autin et al., 2013; Bellahsen and Daniel, 2005; Corti, 2004; Faccenna et al., 1995; Henza et al., 2011, 2010). Oblique kinematics (Withjack & Jamison, 1986) are not required to create extension-oblique faults when the basement is sufficiently anisotropic, and this anisotropy does not have to occur at the whole of lithosphere scale (cf. Agostini et al., 2009; Brune et al., 2017; Corti, 2008).

Our experiments show that the local strain direction indicated by individual faults need not reflect the orthogonal extension boundary condition (analogous to the N-S extension direction in the Gippsland Basin study area). This finding demonstrates the inadequacy of inferring regional extension directions from fault orientations alone and highlights the importance of understanding non-plane strains in rift evolution and passive margin formation (Brune et al., 2018; Dewey et al., 1998).

6. Conclusions

The experimental results presented here describe the control of crustal strength on fault spacing and the length scale-dependent relationship between lower crustal anisotropies and fault behavior in the upper crust during a single phase of rifting. How vertical strength anisotropies in the lower crust influence fault orientations in the upper crust is a function of: (i) scale (i.e., the width and spacing of anisotropies relative to the size of the modelled area), and (ii) the mechanical properties of the individual zones that make up the anisotropic material. Hence the geometry of lower crustal zones of differing strengths may interact with rift kinematics, impacting the orientation, kinematics, and spacing of fault sets developed in a basin. We show that the basement of a rift basin must be sufficiently anisotropic for extension-oblique rift faults to form across a wide area. Additionally, such faults can form oblique to the trend of pre-existing basement anisotropies, demonstrating that pre-existing basement structures/weaknesses can be inherited via a mechanism other than reactivation, which would otherwise result in new faults that are parallel to these basement structures.

Acknowledgments

The authors thank Steven Micklethwaite for helpful discussions during the preparation of this manuscript. A. Samsu was supported by a Monash University Faculty of Science Dean's International Postgraduate Research Scholarship and Postgraduate Publication Award. Data

archiving is underway. Data related to this manuscript are included in the Supporting Information for review purposes and will be made publicly available on monash.figshare.

References

Adam, J., Urai, J. L., Wieneke, B., Oncken, O., Pfeiffer, K., Kukowski, N., et al. (2005). Shear localisation and strain distribution during tectonic faulting—new insights from granular-flow experiments and high-resolution optical image correlation techniques. *Journal of Structural Geology*, *27*(2), 283–301. https://doi.org/10.1016/j.jsg.2004.08.008

Agostini, A., Corti, G., Zeoli, A., & Mulugeta, G. (2009). Evolution, pattern, and partitioning of deformation during oblique continental rifting: Inferences from lithospheric-scale centrifuge models. *Geochemistry, Geophysics, Geosystems*, *10*(11). https://doi.org/10.1029/2009GC002676

Artyushkov, E. V. (1983). *Geodynamics*. Amsterdam: Elsevier.

Autin, J., Bellahsen, N., Leroy, S., Husson, L., Beslier, M. O., & D'Acremont, E. (2013). The role of structural inheritance in oblique rifting: Insights from analogue models and application to the Gulf of Aden. *Tectonophysics*, *607*, 51–64. https://doi.org/10.1016/j.tecto.2013.05.041

Bell, J. S. (1996). Petro geoscience 2. In situ stresses in sedimentary rocks (part 2): Applications of stress measurements. *Geoscience Canada*.

Bellahsen, N., & Daniel, J. M. (2005). Fault reactivation control on normal fault growth: An experimental study. *Journal of Structural Geology*, *27*(4), 769–780. https://doi.org/10.1016/j.jsg.2004.12.003

Benes, V., & Davy, P. (1996). Modes of continental lithospheric extension: Experimental verification of strain localization processes. *Tectonophysics*, *254*(1–2), 69–87. https://doi.org/10.1016/0040-1951(95)00076-3

Benes, V., & Scott, S. D. (1996). Oblique rifting in the Havre Trough and its propagation into the continental margin of New Zealand: Comparison with analogue experiments. *Marine Geophysical Research*, *18*(2–4), 189–201. https://doi.org/10.1007/BF00286077

Boutelier, D., Cruden, A., & Saumur, B. (2016). Density and visco-elasticity of Natrosol 250 HH solutions: Determining their suitability for experimental tectonics. *Journal of Structural Geology*, *86*, 153–165. https://doi.org/10.1016/j.jsg.2016.03.001

Brune, S., Corti, G., & Ranalli, G. (2017). Controls of inherited lithospheric heterogeneity on rift linkage: Numerical and analogue models of interaction between the Kenyan and Ethiopian rifts across the Turkana depression. *Tectonics*, 1–20. https://doi.org/10.1002/2017TC004739

Brune, S., Willliams, S. E., & Müller, R. D. (2018). Oblique rifting: the rule, not the exception. *Solid Earth*, *9*, 1187–1206. https://doi.org/https://doi.org/10.5194/se-9-1187-2018

Byerlee, J. (1978). Friction of rocks. *Pure and Applied Geophysics*, *116*(4–5), 615–626. https://doi.org/10.1007/BF00876528

Cayley, R. A. (2011). Exotic crustal block accretion to the eastern Gondwanaland margin in the Late Cambrian-Tasmania, the Selwyn Block, and implications for the Cambrian-Silurian evolution of the Ross, Delamerian, and Lachlan orogens. *Gondwana Research*, *19*(3), 628–649. https://doi.org/10.1016/j.gr.2010.11.013

Cayley, R. A., Taylor, D. H., VandenBerg, A. H. M., & Moore, D. H. (2002). Proterozoic - Early Palaeozoic rocks and the Tyennan Orogeny in central Victoria: The Selwyn Block and its tectonic implications. *Australian Journal of Earth Sciences*, *49*(2), 225–254. https://doi.org/10.1046/j.1440-0952.2002.00921.x

Constantine, A. (2001). *Sedimentology, Stratigraphy and Palaeoenvironment of the Upper Jurassic-Lower Cretaceous Non-Marine Strzelecki Group, Gippsland Basin, Southeastern Australia*. Monash University. PhD Thesis.

Corti, G. (2004). Centrifuge modelling of the influence of crustal fabrics on the development of transfer zones: Insights into the mechanics of continental rifting architecture. *Tectonophysics*, *384*, 191–208. https://doi.org/10.1016/j.tecto.2004.03.014

Corti, G. (2008). Control of rift obliquity on the evolution and segmentation of the main Ethiopian rift. *Nature Geoscience*, *1*(4), 258–262. https://doi.org/10.1038/ngeo160

Corti, G., van Wijk, J., Cloetingh, S., & Morley, C. K. (2007). Tectonic inheritance and continental rift architecture: Numerical and analogue models of the East African Rift system. *Tectonics*, *26*(6), 1–13. https://doi.org/10.1029/2006TC002086

Cruden, A. R., Nasseri, M. H. B., & Pysklywec, R. (2006). Surface topography and internal strain variation in wide hot orogens from three-dimensional analogue and two-dimensional numerical vice models. *Geological Society Special Publications*, *253*(1), 79–104. https://doi.org/10.1144/GSL.SP.2006.253.01.04

Daly, M. C., Chorowicz, J., & Fairhead, J. D. (1989). Rift basin evolution in Africa: the influence of reactivated steep basement shear zones. *Geological Society, London, Special Publications*, *44*(1), 309–334. https://doi.org/10.1144/GSL.SP.1989.044.01.17

Davy, P., & Cobbold, P. R. (1991). Experiments on shortening of a 4-layer model of the continental lithosphere. *Tectonophysics*, *188*(1–2), 1–25. https://doi.org/10.1016/0040-1951(91)90311-F

Dewey, J., Holdsworth, R., & Strachan, R. (1998). Transpression and transtension zones. *Geological Society, London, Special Publications*, *135*, 1–14.

Duarte, J. C., Schellart, W. P., & Cruden, A. R. (2014). Rheology of petrolatum-paraffin oil mixtures: Applications to analogue modelling of geological processes. *Journal of Structural Geology*, *63*, 1–11. https://doi.org/10.1016/j.jsg.2014.02.004

Etheridge, M. A., Branson, J. C., & Stuart-Smith, P. G. (1985). Extensional basin-forming structures in Bass Strait and their importance for hydrocarbon exploration. *The APEA Journal*, *25*, 344–361.

Faccenna, C., Nalpas, T., Brun, J. P., Davy, P., & Bosi, V. (1995). The influence of pre-existing thrust faults on normal fault geometry in nature and in experiments. *Journal of Structural Geology*, *17*(8), 1139–1149. https://doi.org/10.1016/0191-8141(95)00008-2

Fossen, H., & Tikoff, B. (1998). Extended models of transpression and transtension, and application to tectonic settings. *Geological Society, London, Special Publications*, *135*(1), 15–33. https://doi.org/10.1144/GSL.SP.1998.135.01.02

Gibson, G. M., Totterdell, J. M., White, L. T., Mitchell, C. H., Stacey, A. R., Morse, M. P., & Whitaker, A. (2013). Pre-existing basement structure and its influence on continental rifting and fracture zone development along Australia's southern rifted margin. *Journal of the Geological Society*, *170*(2), 365–377. https://doi.org/10.1144/jgs2012-040

Gray, D. R., Foster, D. A., Gray, C., Cull, J., & Gibson, G. (1998). Lithospheric Structure of the Southeast Australian Lachlan Orogen along the Victorian Global Geoscience Transect. *International Geology Review*, *40*(12), 1088–1117. https://doi.org/10.1080/00206819809465256

Heilman, E., Kolawole, F., Atekwana, E. A., & Mayle, M. (2019). Controls of Basement Fabric on the Linkage of Rift Segments. *Tectonics*. https://doi.org/10.1029/2018TC005362

Henza, A. A., Withjack, M. O., & Schlische, R. W. (2010). Normal-fault development during two phases of non-coaxial extension: An experimental study. *Journal of Structural Geology*, *32*(11), 1656–1667. https://doi.org/10.1016/j.jsg.2009.07.007

Henza, A. A., Withjack, M. O., & Schlische, R. W. (2011). How do the properties of a pre-existing normal-fault population influence fault development during a subsequent phase of extension? *Journal of Structural Geology*, *33*(9), 1312–1324. https://doi.org/10.1016/j.jsg.2011.06.010

Heron, P. J., Peace, A. L., McCaffrey, K., Welford, J. K., Wilson, R., Hunen, J., & Pysklywec, R. N. (2019). Segmentation of rifts through structural inheritance: Creation of the Davis Strait. *Tectonics*, 2019TC005578. https://doi.org/10.1029/2019TC005578

Holdsworth, R. E., Butler, C. A., & Roberts, A. M. (1997). The recognition of reactivation during continental deformation. *Journal of the Geological Society*, *154*(1), 73–78. https://doi.org/10.1144/gsjgs.154.1.0073

Kennett, B. L. N., Fichtner, A., Fishwick, S., & Yoshizawa, K. (2013). Australian seismological referencemodel (AuSREM): Mantle component. *Geophysical Journal International*, *192*(2), 871–887. https://doi.org/10.1093/gji/ggs065

Kirkpatrick, J. D., Bezerra, F. H. R., Shipton, Z. K., Do Nascimento, A. F., Pytharouli, S. I., Lunn, R. J., & Soden, A. M. (2013). Scale-dependent influence of pre-existing basement shear zones on rift faulting: a case study from NE Brazil. *Journal of the Geological Society*, *170*, 237–247. https://doi.org/10.1144/jgs2012-043

Mandl, G., Jong, L. N. J., & Maltha, A. (1977). Shear zones in granular material. *Rock Mechanics*, *9*(2–3), 95–144. https://doi.org/10.1007/BF01237876

McLean, M. A., Morand, V. J., & Cayley, R. A. (2010). Gravity and magnetic modelling of crustal structure in central Victoria: what lies under the Melbourne Zone? *Australian*

Journal of Earth Sciences, *57*(2), 153–173. https://doi.org/10.1080/08120090903416245

Miller, J. M. L., Norvick, M. S., & Wilson, C. J. L. (2002). Basement controls on rifting and the associated formation of ocean transform faults - Cretaceous continental extension of the southern margin of Australia. *Tectonophysics*, *359*(1–2), 131–155. https://doi.org/10.1016/S0040-1951(02)00508-5

Molnar, N. E., Cruden, A. R., & Betts, P. G. (2017). Interactions between propagating rotational rifts and linear rheological heterogeneities: Insights from three-dimensional laboratory experiments. *Tectonics*, *36*(3), 420–443. https://doi.org/10.1002/2016TC004447

Molnar, N. E., Cruden, A. R., & Betts, P. G. (2018). Unzipping continents and the birth of microcontinents. *Geology*, *46*(5), 451–454. https://doi.org/10.1130/G40021.1

Moore, A. M. G., Stagg, H. M. J., & Norvick, M. S. (2000). Deep-water Otway Basin: A new assessment of the tectonics and hydrocarbon prospectivity. *The APPEA Journal*, 66–85.

Moore, D. H., Betts, P. G., & Hall, M. (2016). Constraining the VanDieland microcontinent at the edge of East Gondwana, Australia. *Tectonophysics*, *687*, 158–179. https://doi.org/10.1016/j.tecto.2016.09.009

Morley, C. K. (2010). Stress re-orientation along zones of weak fabrics in rifts: An explanation for pure extension in "oblique" rift segments? *Earth and Planetary Science Letters*, *297*(3–4), 667–673. https://doi.org/10.1016/j.epsl.2010.07.022

Norvick, M. S., & Smith, M. S. (2001). Mapping the plate tectonic reconstruction of southern and southeastern Australia and implications for petroleum systems. *The APPEA Journal*, *41*, 15–35.

Philippon, M., Willingshofer, E., Sokoutis, D., Corti, G., Sani, F., Bonini, M., & Cloetingh, S. (2015). Slip re-orientation in oblique rifts. *Geology*, *43*(2), 147–150. https://doi.org/10.1130/G36208.1

Phillips, T. B., Jackson, C. A. L., Bell, R. E., Duffy, O. B., & Fossen, H. (2016). Reactivation of intrabasement structures during rifting: A case study from offshore southern Norway. *Journal of Structural Geology*, *91*, 54–73. https://doi.org/10.1016/j.jsg.2016.08.008

Power, M. R., Hill, K. C., Hoffman, N., Bernecker, T., & Norvick, M. (2001). The Structural and Tectonic Evolution of the Gippsland Basin: Results from 2D Section Balancing and

3D Structural Modelling. In K. C. Hill & T. Bernecker (Eds.), *Eastern Australasian Basins Symposium* (pp. 373–384).

Power, M. R., Hill, K. C., & Hoffman, N. (2003). Structural inheritance, stress rotation, overprinting and compressional reactivation in the Gippsland Basin - Tuna 3D seismic dataset. *The APPEA Journal*, *43*, 197–221. https://doi.org/https://doi.org/10.1071/AJ02010

Pysklywec, R. N., & Cruden, A. R. (2004). Coupled crust-mantle dynamics and intraplate tectonics: Two-dimensional numerical and three-dimensional analogue modeling. *Geochemistry, Geophysics, Geosystems*, *5*(10). https://doi.org/10.1029/2004GC000748

Ramberg, H. (1967). *Gravity, Deformation and the Earth's Crust, as Studied by Centrifuged Models*. London: Academic Press.

Ranalli, G. (1995). *Rheology of the Earth* (2nd ed.). London: Chapman and Hall.

Ranalli, G. (2001). Experimental tectonics: From Sir James Hall to the present. *Journal of Geodynamics*, *32*(1–2), 65–76. https://doi.org/10.1016/S0264-3707(01)00023-0

Riller, U., Cruden, A. R., Boutelier, D., & Schrank, C. E. (2012). The causes of sinuous crustal-scale deformation patterns in hot orogens: Evidence from scaled analogue experiments and the southern Central Andes. *Journal of Structural Geology*, *37*, 65–74. https://doi.org/10.1016/j.jsg.2012.02.002

Ritter, M. C., Leever, K., Rosenau, M., & Oncken, O. (2016). Scaling the sandbox—Mechanical (dis) similarities of granular materials and brittle rock. *Journal of Geophysical Research: Solid Earth*, *121*(9), 6863–6879. https://doi.org/10.1002/2016JB012915

Samsu, A., Cruden, A. R., Micklethwaite, S., Grose, L., & Vollgger, S. A. (2019). Scale matters: the influence of structural inheritance on fracture patterns. Manuscript submitted for publication.

Samsu, A., Cruden, A. R., Hall, M., Micklethwaite, S., & Denyszyn, S. W. (2019). The influence of basement faults on local extension directions: Insights from potential field geophysics and field observations. *Basin Research*, *31*(4), 782–807. https://doi.org/10.1111/bre.12344

Schellart, W. P. (2000). Shear test results for cohesion and friction coefficients for different granular materials: Scaling implications for their usage in analogue modelling. *Tectonophysics*, *324*(1–2), 1–16. https://doi.org/10.1016/S0040-1951(00)00111-6

Schueller, S., & Davy, P. (2008). Gravity influenced brittle-ductile deformation and growth faulting in the lithosphere during collision: Results from laboratory experiments. *Journal of Geophysical Research: Solid Earth*, *113*(12), 1–21. https://doi.org/10.1029/2007JB005560

Sharples, W., Moresi, L.-N., Jadamec, M. A., & Revote, J. (2015). Styles of rifting and fault spacing in numerical models of crustal extension. *Journal of Geophysical Research: Solid Earth*, *120*, 4379–4404. https://doi.org/10.1002/2014JB011813.Received

Tommasi, A., & Vauchez, A. (2001). Continental rifting parallel to ancient collisional belts: an effect of the mechanical anisotropy of the lithospheric mantle. *Earth and Planetary Science Letters*, *185*(1–2), 199–210. https://doi.org/10.1016/S0012-821X(00)00350-2

Wijns, C., Weinberg, R., Gessner, K., & Moresi, L. (2005). Mode of crustal extension determined by rheological layering. *Earth and Planetary Science Letters*, *236*, 120–134. https://doi.org/10.1016/j.epsl.2005.05.030

Willcox, J. B., & Stagg, H. M. J. (1990). Australia’s southern margin: a product of oblique extension. *Tectonophysics*, *173*, 269–281. https://doi.org/10.1016/0040-1951(90)90223-U

Willcox, J. B., Colwell, J. B., & Constantine, A. E. (1992). New ideas on Gippsland Basin regional tectonics. In *Gippsland Basin Symposium 22-23 June 1992* (pp. 93–110). Melbourne.

Wilson, J. T. (1966). Did the Atlantic Close and then Re-open? *Nature*, *211*, 676–681.

Wilson, R. W., Holdsworth, R. E., Wild, L. E., McCaffrey, K. J. W., England, R. W., Imber, J., & Strachan, R. A. (2010). Basement-influenced rifting and basin development: a reappraisal of post-Caledonian faulting patterns from the North Coast Transfer Zone, Scotland. *Geological Society, London, Special Publications*, *335*(1), 795–826. https://doi.org/10.1144/SP335.32

Withjack, M., & Jamison, W. R. (1986). Deformation produced by oblique rifting. *Tectonophysics*, *126*, 99–124. https://doi.org/https://doi.org/10.1016/0040-1951(86)90222-2

Zwaan, F., & Schreurs, G. (2017). How oblique extension and structural inheritance influence rift segment interaction: Insights from 4D analog models. *Interpretation*, *5*(1), SD119–SD138. https://doi.org/10.1190/INT-2016-0063.1